

# Enhanced Dynamic Operation of Heavily Saturated IPMSM in Signal-Injection Sensorless Control with Ancillary Reference Frame

Inhwi Hwang, *Student Member, IEEE*, Yong-Cheol Kwon, *Member, IEEE*, Seung-Ki Sul, *Fellow, IEEE*

**Abstract**— This paper proposes a signal-injection sensorless control (SISC) algorithm with enhanced dynamic performance for heavily saturated interior permanent-magnet synchronous motors (IPMSMs). Considering the magnetic saturations and spatial harmonics of IPMSM, the convergence characteristics of SISC algorithms are analyzed. To improve dynamic performance of SISC, ancillary angles including voltage injection angle and current observation angle are employed. Additionally, position observer's pole placements of the proposed method are also analyzed with root-loci to set the proper input gain of the observer. For the optimization of the proposed method, a performance index defined in this paper which represents the convergence performance of the proposed method should be maximized. This index implies both characteristics of the effective signal magnitude and the convergence range. To implement the proposed method, high frequency inductances, ancillary angles, and compensation current should be extracted, and all of the extraction methods are specified with a flowchart. The superiority of the proposed method is verified with simulations and experiments under various speeds with stepwise high torque.

**Index Terms**—Signal-injection sensorless control (SISC), permanent-magnet synchronous motor, finite element analysis (FEA), ancillary angles, convergence analysis.

## I. INTRODUCTION

In the traction applications, sensorless control algorithms have been considered as a backup algorithm against the sudden failure of the position sensor. This improves system reliability, reduce overall system volume, and cut down system cost. The sensorless control algorithms can be divided into signal-injection sensorless control (SISC) based on intentionally injected high-frequency (HF) voltage/current [1], [21] and model-based sensorless control [2]-[3] that utilizes fundamental voltage/current components used for control of the motor. SISC is mainly used at a low speed and standstill. On the other hand, when the rotor speed is high enough, a model-based sensorless method has been broadly used for estimating the rotor position. Under a low speed and stationary condition, it is hard to estimate the rotor position due to the inferior quality of the electromotive force (EMF) [27].

In SISC, the rotor position can be estimated with current response to HF voltage which is superimposed on the fundamental voltage. HF current signal is a function of HF inductances and position estimation error. Various kinds of voltage injection method have been reported such as sinusoidal and square types. With sinusoidal voltage injection, injection frequencies around 700 Hz ~ 1 kHz are utilized, which limits the bandwidths of controllers and observers [21], [29]-[31]. However, the square wave injection method enables much faster response of the position estimation thanks to its much higher injection frequency, making it possible to increase bandwidths of controllers and observers [1].

Meanwhile, it has already been known that the position estimation capability of SISC can be deteriorated and lost in heavy loading condition [4]-[5], [32]. In this condition, the iron core of interior permanent-magnet synchronous motors (IPMSMs) could be highly saturated by the magnetic flux induced by the stator current. Thus, the spatial magnetic flux distribution would be reshaped undesirably. Accordingly, the HF inductances vary as the current operating point varies. This phenomenon casts doubt on the reliability of conventional modeling assuming the HF inductance as fixed parameters regardless of actual current operating point. Therefore, there had been efforts to establish more reliable sensorless control method considering the variation of HF inductance [14]. As the magnetic flux of the motor is highly saturated, the effect of the cross-saturation becomes greater, which results in displacement of the convergence point [22]-[25].

For these reasons, sensorless operation in the higher torque region was considered impossible with the conventional analysis. Therefore, it was essential to determine the maximum operable torque point of SISC [6]-[8], and there were also efforts to change the shape of a motor to overcome the torque limitation [9]-[10]. In addition, input disturbance analysis of SISC observer was also conducted. It was identified that the main factors of the disturbance were the dead-time and the voltage drop of the switching element [11]-[12].

---

This work was supported by the Seoul National University Electric Power Research Institute (SEPRI).

Table I. Features of conventional SISC methods and the proposed method.

Applied control method	Jang <i>et al.</i> [21]	Yoon <i>et al.</i> [1]	Li <i>et al.</i> [14]	Lee <i>et al.</i> [13]	Kwon <i>et al.</i> [17]	Lee <i>et al.</i> [18]	Varatharajan <i>et al.</i> [20]	This paper
Cross-saturation compensation	X	X	O	O	O	O	O	O
Spatial harmonics compensation	X	X	X	O	O	O	X	O
HF voltage injection angle tilting	X	X	X	X	O	X	O	O
Current reference angle tilting	X	X	X	X	X	O	X	X
HF current observation angle tilting	X	X	X	X	X	X	X	O

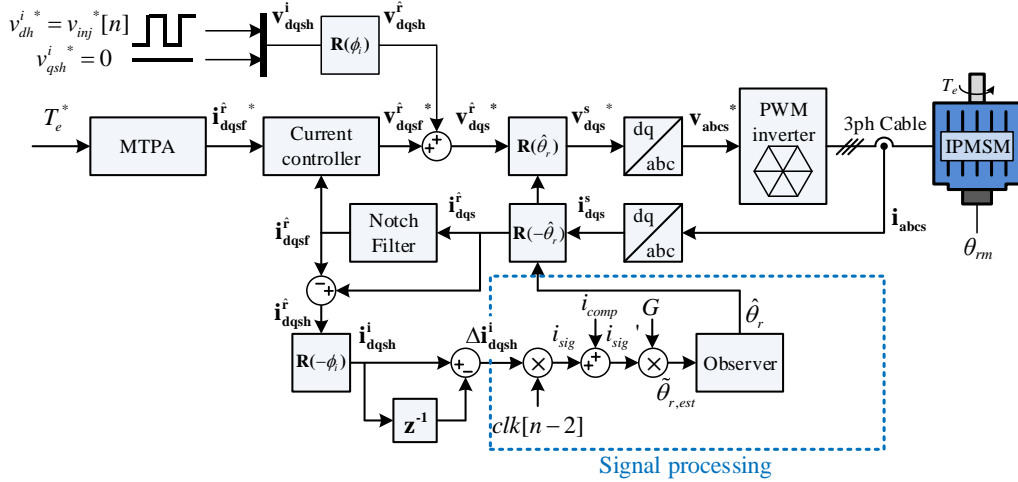


Fig. 1. Conventional SISC system block diagram [17].

Some methods have been proposed for more robust SISC in the high torque region. For instance, a SISC algorithm with compensation of the offset error in the position tracking was proposed in [13]-[16]. Also, it had been proposed that HF voltage was injected not in the  $d$ -axis of the estimated rotor reference frame (ERRF) but in the  $d$ -axis of the tilted reference frame in [17]. Moreover, the  $q$ -axis of a tilted reference frame is exploited to get an error signal. The SISC performance was improved by tilting the current reference without tilting the signal injection angle in [18]. These methods [17]-[18] could conspicuously improve the torque capability of IPMSM in SISC. However, the position tracking with the above methods can become unstable or marginally stable in highly dynamic operating condition since they mainly focus on the steady-state stability of SISC. In addition, there were no mentions of how to extract the compensation tables, such as tilted angles in [17]-[18]. Moreover, the  $q$ -axis current signal has been mainly used since it typically contains a large effective signal for SISC in the conventional SISC methods. However, even with the large signal the aforementioned dynamic performance degradation happens in the case of heavily saturated IPMSMs.

Similar methodologies were also employed in [19]-[20]. The authors in [19] took the effect of cross-saturation into account to eliminate position tracking error by adding HF differential current component in  $d$ -axis to that in  $q$ -axis and using it as an error signal. However, they did not consider the inductance variation according to the position error. In contrast, authors in [20] dealt with the variation of the inductance according to the position error, and they also used the injection tilting method in

heavy loading condition. However, they all ignored the impact of spatial harmonics on HF inductance in a highly saturated condition.

Table I compares various SISC methods according to their control strategies.

This paper proposes a SISC method that can improve the position tracking characteristics in dynamic transient by maximizing effective signal embedding the position information. In the proposed method, two ancillary angles are exploited to enlarge the magnitude of the effective signal. Furthermore, the newly defined variable gain connecting the HF current to the angle error, the input to the angle tracking observer, could reflect the variation of dynamic inductances in the heavily saturated IPMSM. Moreover, a look-up table extraction method used in the proposed method is also introduced by establishing and optimizing ‘performance index’, which represents the tracking performance of a given SISC algorithm.

## II. CONVENTIONAL METHOD

The HF voltage equation of IPMSM can be formulated as follows:

$$\begin{aligned} \begin{bmatrix} v_{dsh}^r \\ v_{qsh}^r \end{bmatrix} &= \mathbf{L}_h \frac{d}{dt} \begin{bmatrix} i_{dsh}^r \\ i_{qsh}^r \end{bmatrix} \\ &= \begin{bmatrix} L_{dh} & L_{dqh} \\ L_{qdh} & L_{qh} \end{bmatrix} \frac{d}{dt} \begin{bmatrix} i_{dsh}^r \\ i_{qsh}^r \end{bmatrix} = \begin{bmatrix} \frac{\partial \lambda_{ds}^r}{\partial i_{ds}^r} & \frac{\partial \lambda_{ds}^r}{\partial i_{qs}^r} \\ \frac{\partial \lambda_{qs}^r}{\partial i_{ds}^r} & \frac{\partial \lambda_{qs}^r}{\partial i_{qs}^r} \end{bmatrix} \frac{d}{dt} \begin{bmatrix} i_{dsh}^r \\ i_{qsh}^r \end{bmatrix}. \end{aligned} \quad (1)$$

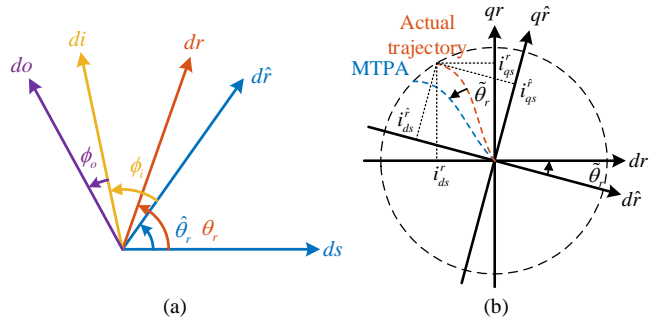


Fig. 2. (a) Definition of angles and axes. (b) Actual and desired MTPA curve with respect to position error.

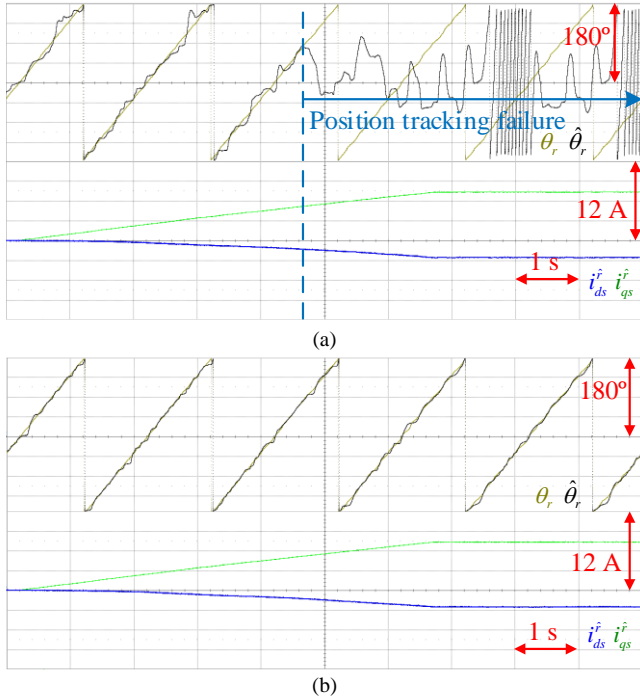


Fig. 3. Comparison of SISC performance with slowly increasing torque command. (a) Failure of position tracking due to cross-saturation with conventional method [1]. (b) Position tracking control with advanced method [17].

Table II. Specification of target IPMSM.

Pole/Slot	6/9
DC link voltage	300 V
Number of phases	3
Stator resistance	0.58 \$\Omega\$
Rated torque	1.17 N\$\cdot\$m
Rated current	2.85 A <sub>rms</sub>
Rated speed	3000 r/min
Maximum speed	4500 r/min
Flux linkage of the magnet	63 mWb-t
Nominal \$d\$-axis inductance	7.13 mH
Nominal \$q\$-axis inductance	11.04 mH

In (1),  $v$  stands for voltage,  $i$  for current,  $L$  for inductance, and  $\lambda$  for magnetic flux. The superscript ' $r$ ' means the rotor reference frame (RRF), the subscript ' $s$ ' stands for the stator component, and ' $h$ ' for the HF component.  $\mathbf{L}_h$  is the dynamic inductance matrix, the partial derivative of the magnetic flux regarding the current. Eq. (1) holds under that assumption that the HF resistance is negligible compared to the HF reactance [26], [28].

$i_{dsh}^r$  and  $i_{qsh}^r$  are obtained from the output of the notch filter used for SISC signal processing.

Fig. 1 shows a control block diagram of the conventional SISC system [17] that is the background of this paper. In this paper, square-wave type voltage injection [1] is used for SISC.

Fig. 2 (a) depicts various angles and axes for discussion in this paper. In the figure,  $\theta_r$  stands for the rotor position,  $\hat{\theta}_r$  for the estimated rotor position, and  $\tilde{\theta}_r$  for the position error. Note that the actual current is not the same as the current reference in Fig. 2(b) if  $\tilde{\theta}_r$  is not zero. The actual operating point changes as  $\tilde{\theta}_r$  varies, which inevitably results in the variation of the HF inductance and torque discrepancy. In addition, there are two ancillary angles,  $\phi_i$ , and  $\phi_o$  in Fig. 2(a).  $\phi_i$  is the ancillary injection angle defined in [17].  $\phi_o$  is the ancillary observation angle defined in this paper which will be discussed in chapter III. 'ds' is the  $d$ -axis of stationary reference frame, ' $dr$ ' is that of RRF, ' $di$ ' and ' $do$ ' are those of ancillary injection and observation reference frames (AIRF and AORF) introduced in this paper. The superscript ' $i$ ' and ' $o$ ' represent AIRF and AORF, respectively.

In AIRF, HF injection voltage reference  $v_{dqsh}^{i*}$  can be expressed as follows:

$$v_{dqsh}^{i*}[n] = \begin{bmatrix} v_{inj}^{i*}[n] \\ 0 \end{bmatrix} = \begin{bmatrix} V_h \cdot clk[n] \\ 0 \end{bmatrix}, \quad (2)$$

where  $V_h$  is the amplitude of injection voltage and

$$clk[n] = \begin{cases} 1 & \text{when } n \text{ is odd} \\ -1 & \text{else} \end{cases} \quad (3)$$

is a pulsating signal with the value of  $\pm 1$ .  $v_{dqsh}^{i*}$  is applied to the motor through the inverter using pulse width modulation (PWM). The current variation of HF current component at  $n$  sampling instant in AIRF induced by the corresponding HF voltage,  $\Delta i_{dqsh}^i[n] \triangleq i_{dqsh}^i[n] - i_{dqsh}^i[n-1]$ , can be derived as follows:

$$\Delta i_{dqsh}^i[n] = \begin{bmatrix} \Delta i_{ds}^i[n] \\ \Delta i_{qs}^i[n] \end{bmatrix} = \begin{bmatrix} I_\Sigma + I_\Delta \cos(2\tilde{\theta}_r - 2\phi_\Delta - 2\phi_i) \\ I_\Delta \sin(2\tilde{\theta}_r - 2\phi_\Delta - 2\phi_i) \end{bmatrix} \cdot clk[n-2], \quad (4)$$

where

$$I_\Sigma = \frac{V_h T_s \sum L_h}{L_{dh} L_{qh} - L_{dqh}^2}, \quad (5)$$

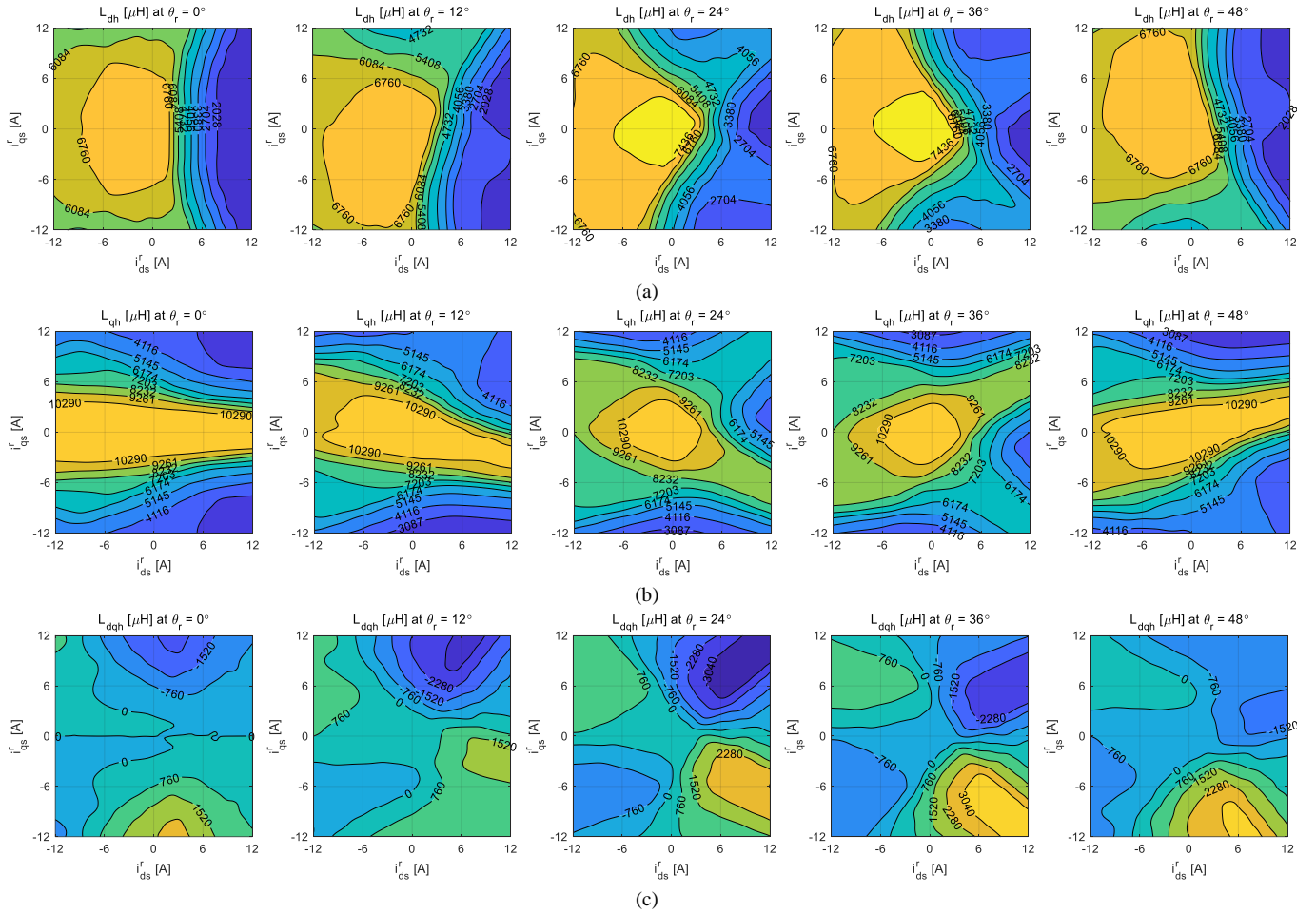
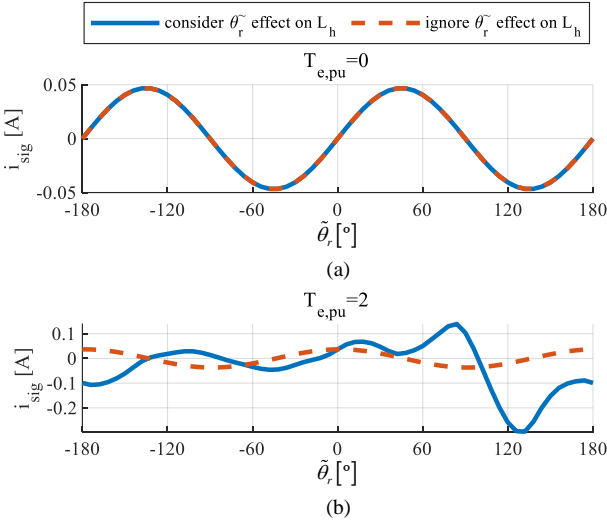
$$I_\Delta = \frac{V_h T_s \sqrt{L_{dqh}^2 + \Delta L_h^2}}{L_{dh} L_{qh} - L_{dqh}^2}, \quad (6)$$

$$\text{and } \phi_\Delta = \frac{1}{2} \text{atan}2(L_{dqh}, -\Delta L_h). \quad (7)$$

In (5)-(7),  $\sum L_h \triangleq \frac{1}{2}(L_{dh} + L_{qh})$  and  $\Delta L_h \triangleq \frac{1}{2}(L_{dh} - L_{qh})$ .  $clk$  should be removed to extract the angular error information from  $\Delta i_{dqsh}^i$ . For this,  $\Delta i_{qs}^i[n]$  in (4) is multiplied by  $clk[n-2]$  to obtain  $i_{sig}$  as follows:

$$i_{sig} = \Delta i_{qs}^i \cdot clk[n-2]. \quad (8)$$

In [1], the HF voltage is injected into the  $d$ -axis in the RRF, i.e.,  $\phi_i = 0$ , and the HF  $q$ -axis current signal is extracted by a band-pass filter (BPF). If the effect of cross-saturation is negligible,  $i_{sig}$  can be approximated as follows:

Fig. 4. (a)  $L_{dh}$ , (b)  $L_{qh}$ , and (c)  $L_{dqh}$  contours of target IPMSM (FEA).Fig. 5. (a)  $i_{sig}$  curves of IPMSM according to  $\tilde{\theta}_r$  with  $T_e^* = 0$  pu, (b) 2 pu ( $\theta_r = 0^\circ$ , and  $\phi_i = 0^\circ$ ).

$$i_{sig} \approx \frac{V_h T_s |\Delta L_h|}{L_{dh} L_{qh}} \sin(2\tilde{\theta}_r) \quad (9)$$

By linear approximation at  $\tilde{\theta}_r = 0$ , an estimated value of  $\tilde{\theta}_r$ ,

$\tilde{\theta}_{r,est}$ , can be obtained as follows:

$$\tilde{\theta}_{r,est} \approx \frac{L_{dh} L_{qh}}{2V_h T_s |\Delta L_h|} i_{sig} \quad (10)$$

Fig. 3(a) shows typical waveforms under sensorless torque control with slowly increasing torque command from 0 pu to 2 pu torque[1]. The specification of the target IPMSM is shown in Table II. When the torque reference is over 1.5 pu at 4.7 s, position tracking fails and estimated position diverges. While, as shown in Fig. 3(b), this problem can be solved by tilting  $\phi_i$  in the high torque region where the motor is heavily saturated.

Fig. 4 shows HF inductances of IPMSM according to  $i_{ds}^r$ ,  $i_{qs}^r$ , and  $\theta_r$  extracted by a finite element analysis (FEA). The FEA has been performed on JMAG Designer 18.0. The HF inductances are not constant values, and they rather continuously vary depending on the operating point in the  $d$ - $q$  current plane. For this reason, the fixed parameter model used in [1] would have limitations in torque control at the high torque region. Because of the low-speed operation, loss components such as stator and rotor core losses and eddy current loss are not considered in the figure. Owing to 60° periodicity in spatial harmonics of the IPMSM, the flux maps are shown for 0-48° rotor position in 12°. The HF inductances of the motor are not constant as assumed in [1], rather they varied according to the rotor position and the stator current. Due to the non-ideal nature of the motor, it is impossible to estimate rotor position with SISC in [1] under high-torque operation.

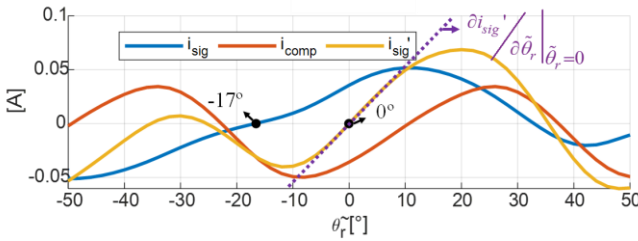


Fig. 6. Convergence point manipulation with  $i_{comp}$ . ( $T_e^*=2$  pu,  $\theta_r=0^\circ$ , and  $\phi_i=0^\circ$ ).

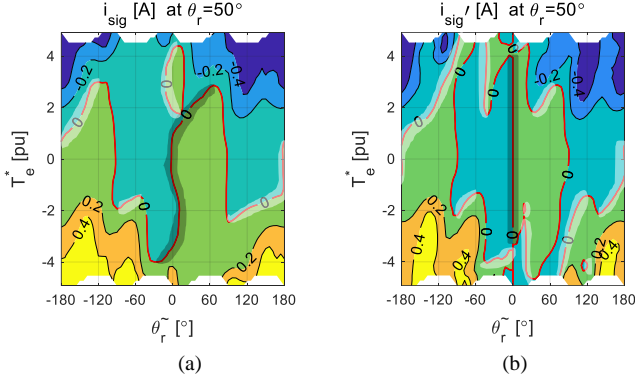


Fig. 7. (a) Contour maps of  $i_{sig}$  and (b)  $i_{sig}'$  ( $\theta_r=50^\circ$ , and  $\phi_i=0^\circ$ ).

Fig. 5 demonstrates how the variation of HF inductance by  $\tilde{\theta}_r$  variation affects  $i_{sig}$ . The orange line is drawn to fix the HF inductances with an operating point  $\tilde{\theta}_r=0^\circ$ , but the blue line is drawn considering the variation of HF inductance. With  $T_e^*=0$  pu, there is no difference between the two graphs. However, at  $T_e^*=2$  pu, they show different graphs. This is because there is a distortion of flux distribution according to  $\tilde{\theta}_r$  due to the large stator current.

After that, the following compensation current (i.e.,  $i_{comp}$ ) was introduced to eliminate the offset error [13]. Then, in order to widen the available torque limit as shown in Fig. 3(b), the injection angle is tilted according to the torque reference [17].  $i_{comp}$  is expressed as follows:

$$i_{comp}(T_e^*, \tilde{\theta}_r) = -i_{sig}(T_e^*, \tilde{\theta}_r = 0, \theta_r = \tilde{\theta}_r), \quad (11)$$

where  $T_e^*$  means the torque command.

$i_{comp}$  is added to  $i_{sig}$  to form  $i_{sig}'$  as follows:

$$i_{sig}' = i_{sig} + i_{comp}. \quad (12)$$

Dividing  $i_{sig}'$  by  $2I_\Delta$ ,  $\tilde{\theta}_{r,est}$  can be obtained as follows:

$$\tilde{\theta}_{r,est} = \frac{i_{sig}'}{2I_\Delta}. \quad (13)$$

$\tilde{\theta}_{r,est}[n]$  is used as the input to the observer. Then, the following expression would holds:

$$\tilde{\theta}_{r,est}(\tilde{\theta}_r = 0) = \frac{i_{sig}'(\tilde{\theta}_r = 0)}{2I_\Delta} = 0. \quad (14)$$

In addition, if the derivative of  $\tilde{\theta}_{r,est}$  at  $\tilde{\theta}_r = 0$  is positive (zero-up crossing condition) as follows:

$$\left. \frac{\partial \tilde{\theta}_{r,est}}{\partial \tilde{\theta}_r} \right|_{\tilde{\theta}_r=0} > 0 \quad (15)$$

,  $\tilde{\theta}_r = 0$  point is the desired convergence point.

Fig. 6 shows  $i_{sig}$ ,  $i_{comp}$ , and  $i_{sig}'$  as an example. If  $i_{sig}$  is used as an input of position observer, the convergence point is placed at  $\tilde{\theta}_r = -17^\circ$ , which causes torque discrepancy. However, if  $i_{sig}'$  is used for SISC, the convergence point is moved to  $0^\circ$ . Likewise, the convergence point can be manipulated by  $i_{comp}$  in the entire torque regions and rotor positions.

Fig. 7 depicts the contours of  $i_{sig}$  and  $i_{sig}'$  with  $\theta_r = 50^\circ$ . The red lines in the contours indicate the zero level points. In the figure, the major convergence points are the points that reach out from the desired convergence point with  $T_e^*=0$ , which is near  $\tilde{\theta}_r = 0$ . The major convergence points are overlaid gray shadow on the top of the red line in Fig. 7. The other convergence points are called the minor ones overlaid white shadow on the top of the red line in Fig. 7. The major convergence point in Fig. 7(a) goes far from the  $\tilde{\theta}_r = 0$  line as  $T_e^*$  increases, due to the large variation of HF inductance. However, the major convergence points can be manipulated to the desired point as shown in Fig. 7(b) by using  $i_{comp}$  [13]. This method is essential to keep zero error in SISC even if the ancillary angles are tilted.

In Fig. 8, contour maps of  $i_{sig}'$  show convergence characteristics of IPMSM in the entire torque region for different rotor positions with the conventional method [17]. Red lines in the contour are points where  $i_{sig}'$  is zero. The major convergence points are on the  $\tilde{\theta}_r = 0$  line, a set of target convergence points with a zero up-crossing condition. However, minor convergence points zero up-crossing but not on  $\tilde{\theta}_r = 0$  line also exist. A convergence range is an interspace between the boundaries of the zero down-crossings of  $i_{sig}'$ , including a major convergence point. Within the convergence range,  $\tilde{\theta}_r$  can converge toward the major convergence point by the negative feedback of the position tracking observer. However, according to Fig. 8, the minor convergence points are observed in the vicinity of the major convergence points with  $T_e^* = \pm 2$  pu. The nearest minor convergence points from the  $\tilde{\theta}_r = 0$  line exist in the region A (red box) and B (blue box) marked in Fig. 8. If  $\tilde{\theta}_r$  converges to the minor convergence point in A due to disturbances, it can diverge along to the minor convergence point as the rotor rotates in the negative direction with  $T_e^* = 2$  pu, as expressed with the pink arrows. The case with  $T_e^* = -2$  pu can also be explained similarly with the blue arrows. Therefore, it is essential for  $\tilde{\theta}_r$  not to fall into the minor convergence points for position tracking.

Fig. 9 demonstrates a simulation result of torque control with conventional SISC. In this simulation, the mechanical rotor speed is 200 r/min with  $\pm 2$  pu torque command. At the beginning of region 1, torque command is applied with  $T_e^* = 2$  pu. In region 1,  $\hat{\theta}_r$  chases  $\theta_r$  well despite the minor convergence point, near the major convergence point, as shown in Fig. 8. Since the rotor rotates in the positive direction, the minor convergence point moves towards the major convergence point. Therefore, even if  $\tilde{\theta}_r$  was trapped by the minor convergence point, it is kept stable near the major convergence point.

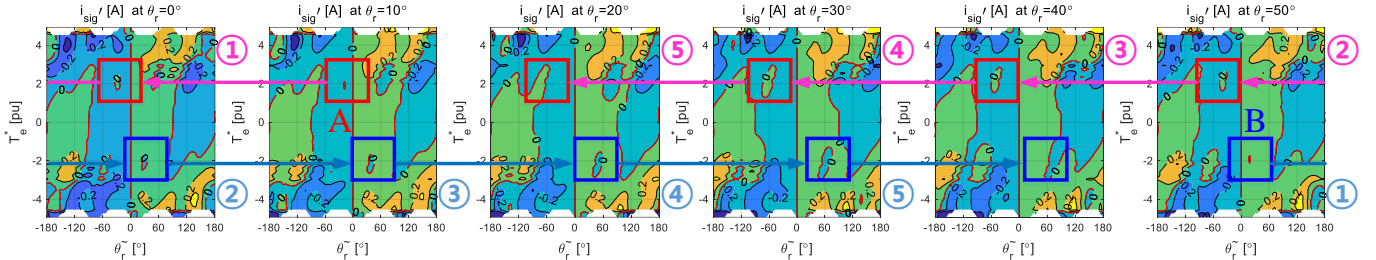
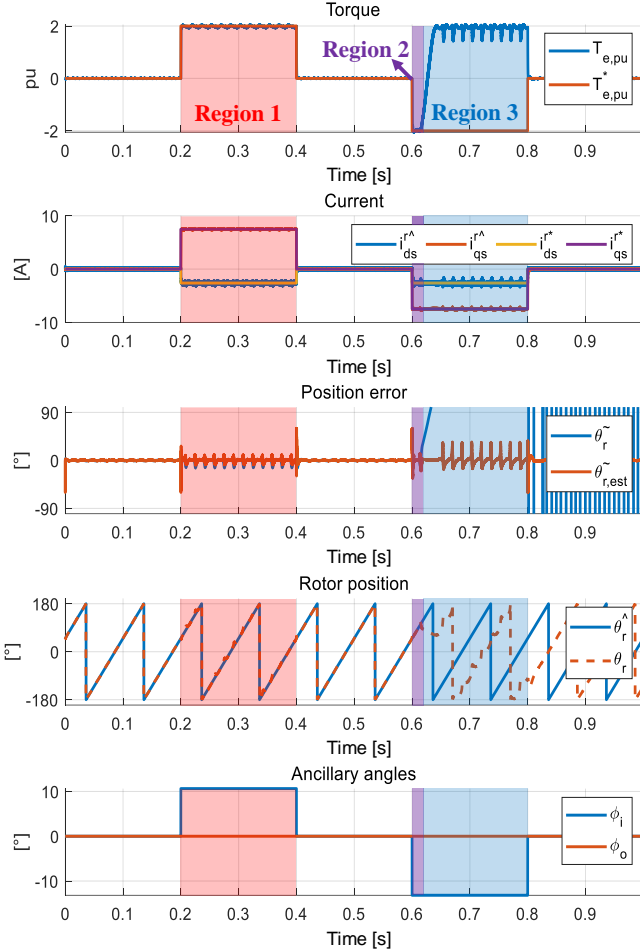
Fig. 8. Contour maps of  $i_{sig}'$  with conventional SISC method [17].

Fig. 9. Torque control simulation result with conventional SISC [17].

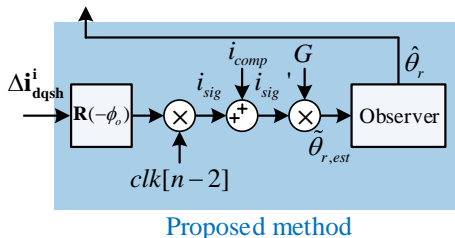
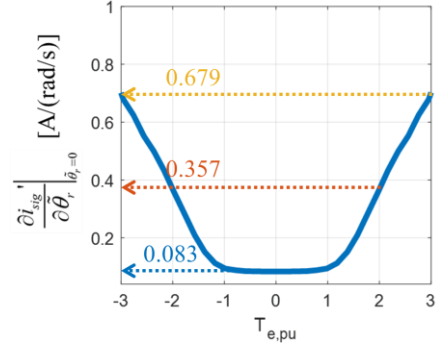
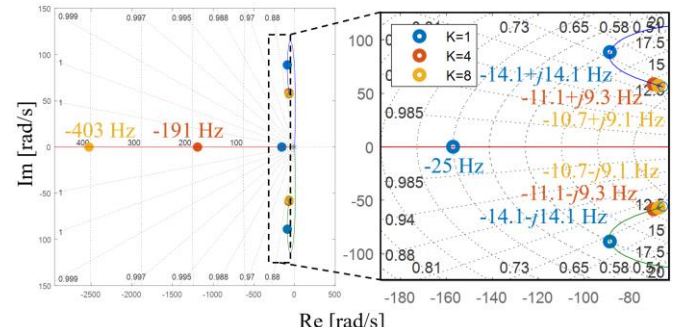


Fig. 10. Proposed SISC system block diagram.

However, in region 2,  $\hat{\theta}_r$  diverges and re-converges to the minor convergence point, and SISC fails in region 3. In this way, the divergence behavior in SISC is determined by the operating point and the rotating direction.

Fig. 11. Slope of  $i_{sig}'$  at the desired convergence point ( $\tilde{\theta}_r = 0$ ) according to torque reference for the target motor.Fig. 12. Actual pole placement of Luenberger observer on root loci when  $\tilde{\theta}_{r,est} = K\tilde{\theta}_r$ .

### III. PROPOSED METHOD

#### A. Signal-Injection Sensorless Control with Ancillary Observation Reference Frame

This paper proposes a SISC method to place the minor convergence points as far as possible from the  $\tilde{\theta}_r = 0$  line by exploiting both  $\phi_i$  and  $\phi_o$ .

Fig. 10 shows the signal processing method of the proposed SISC, and the signal processing block of the conventional SISC in Fig. 1 is replaced with that of Fig. 10. It has two significant differences compared to the conventional method [17]. First, the proposed method uses the  $q$ -axis component of the HF current signal in AORF, which is newly proposed in this paper.

The HF current signal in AORF can be expressed as

$$\begin{aligned} \Delta i_{dqsh}^o[n] &= \mathbf{R}(-\phi_o) \Delta i_{dqsh}^i[n] \\ &= \begin{bmatrix} I_\Sigma \cos \phi_o + I_\Delta \cos(2\tilde{\theta}_r - 2\phi_\Delta - 2\phi_i - \phi_o) \\ -I_\Sigma \sin \phi_o + I_\Delta \sin(2\tilde{\theta}_r - 2\phi_\Delta - 2\phi_i - \phi_o) \end{bmatrix} \cdot clk[n-2]. \end{aligned} \quad (16)$$

$i_{sig}$  in the proposed method can be obtained as follows:

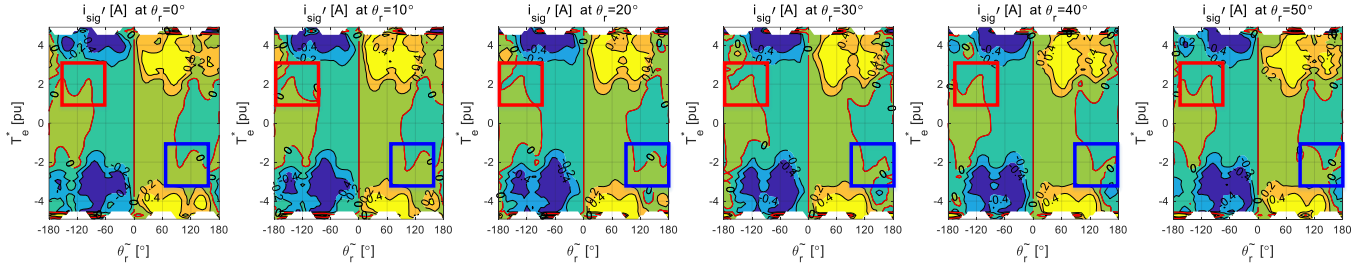
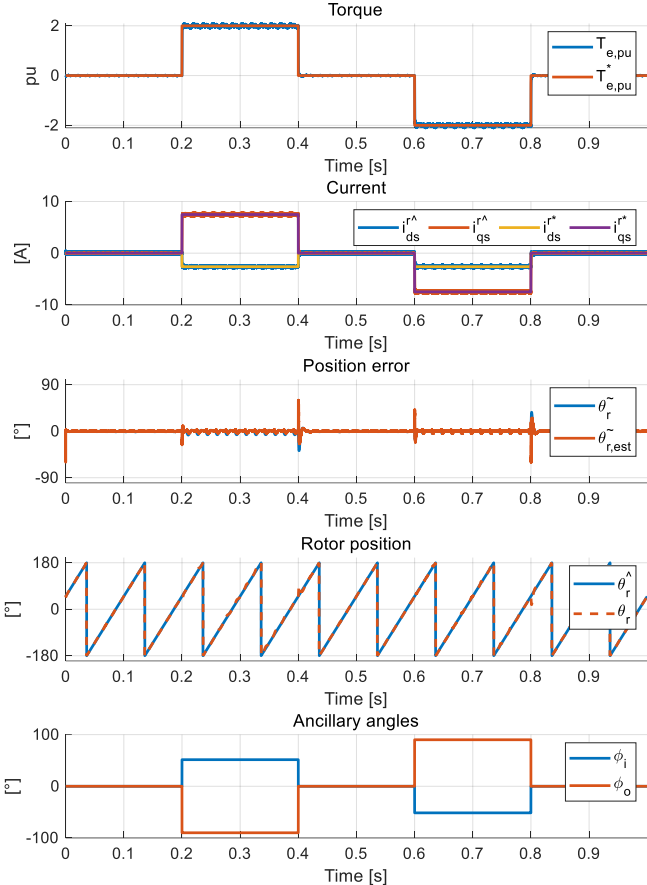
Fig. 13. Contour maps of  $i_{sig}'$  with proposed SISC.

Fig. 14. Torque control simulation result with proposed SISC.

$$i_{sig} = \Delta i_{qsh}^o \cdot clk[n-2] \quad (17)$$

where  $\Delta i_{qsh}^o$  is the difference value of the HF  $q$ -axis current in AORF. Since the major convergence point is manipulated by adding  $i_{comp}$  with (11),  $i_{sig}'$  itself can highly optimize convergence characteristics. Next, the gain  $G$  multiplied on  $i_{sig}'$  is newly defined as follows:

$$\tilde{\theta}_{r,est} = G \cdot i_{sig}' \approx \tilde{\theta}_r \quad (18)$$

where

$$G = \left( \frac{\partial i_{sig}'}{\partial \tilde{\theta}_r} \Big|_{\tilde{\theta}_r=0} \right)^{-1}. \quad (19)$$

$i_{sig}'$  was linearly approximated to  $\tilde{\theta}_{r,est}$  with gain of  $\frac{1}{2I_\Delta}$  in the conventional method [17]-[18]. However, the slope of  $\tilde{\theta}_{r,est}$  is affected not only by  $i_{comp}$  but also by the  $\phi_i$  and  $\phi_o$  term.

Therefore, the gain  $G$  defined as (19) is used in the proposed method instead of  $\frac{1}{2I_\Delta}$  to precisely approximate the  $\tilde{\theta}_{r,est}$  to  $\tilde{\theta}_r$ .

The gain  $G$  can be derived with  $i_{sig}'$  data. In the  $i_{sig}'$  vs  $\tilde{\theta}_r$  graph such as Fig. 6, the inverse of the differential value of  $i_{sig}'$  at  $\tilde{\theta}_r = 0$  is  $G$ . Although  $i_{sig}'$  varies depending on  $\theta_r$ , average value of  $G$  is chosen for the simplicity. Hence,  $G$  is an only function of  $T_e^*$ . If the gain  $G$  is calculated with fixed inductance, the bandwidth of the position observer cannot be kept consistently as designed. This is because  $\frac{\partial i_{sig}'}{\partial \tilde{\theta}_r} \Big|_{\tilde{\theta}_r=0}$  of the motor varies severely by more than 8 times when the torque command increases from 0 pu to 3 pu as shown in Fig. 11.

For the sensorless tracking observer in Fig. 10, Luenberger observer is widely used. Fig. 12 depicts root loci of the Luenberger observer with increasing the input gain of  $\tilde{\theta}_r$ . Initially designed poles are placed to -25 Hz and  $-14 \pm j14$  Hz. The change of the input gain is equivalent to the change of the internal PID gain. It means that if the input gain were not maintained as unity, it results in the migration of the poles. Actual poles of the observer should be fixed in order to keep the stability margin and dynamics of the observer as it was designed. Therefore,  $G$  should be varied according to  $T_e^*$ .

In Fig. 13, it can be seen that the minor convergence points in the proposed method are further moved away from the  $\tilde{\theta}_r = 0$  line than those in the conventional method in Fig. 8. Each red and blue square box indicates the minor convergence points with  $T_e^* = 2$  pu and -2 pu each. Regardless of torque and rotor position, the distance between the  $\tilde{\theta}_r = 0$  line and the minor convergence points is over 80° in the proposed method, which is distinctively larger compared to the conventional method. Therefore, the torque control in SISC would be much more robust to the disturbances coming from a severe load torque disturbance, measurement noise, and inverter nonlinearity.

Fig. 14 demonstrates torque control simulation with the proposed SISC. In contrast to the simulation results with conventional SISC in Fig. 9,  $\hat{\theta}_r$  is well matched to  $\theta_r$  even with  $T_e^* = -2$  pu. The stability of SISC is guaranteed in this simulation.

Fig. 15 shows a flowchart describing how to implement the proposed method. In the figure,  $T_{e,min}^*$  and  $T_{e,max}^*$  mean minimum and maximum available torque command of the target motor, respectively. There are three main processes. *Phase I* is constructing HF inductance data of the target motor. *Phase II* is extracting the appropriate  $\phi_i$  and  $\phi_o$ . *Phase III* is deriving the  $i_{comp}$  with experiment. In the next chapter, detailed implementation methods at each phase will be discussed.

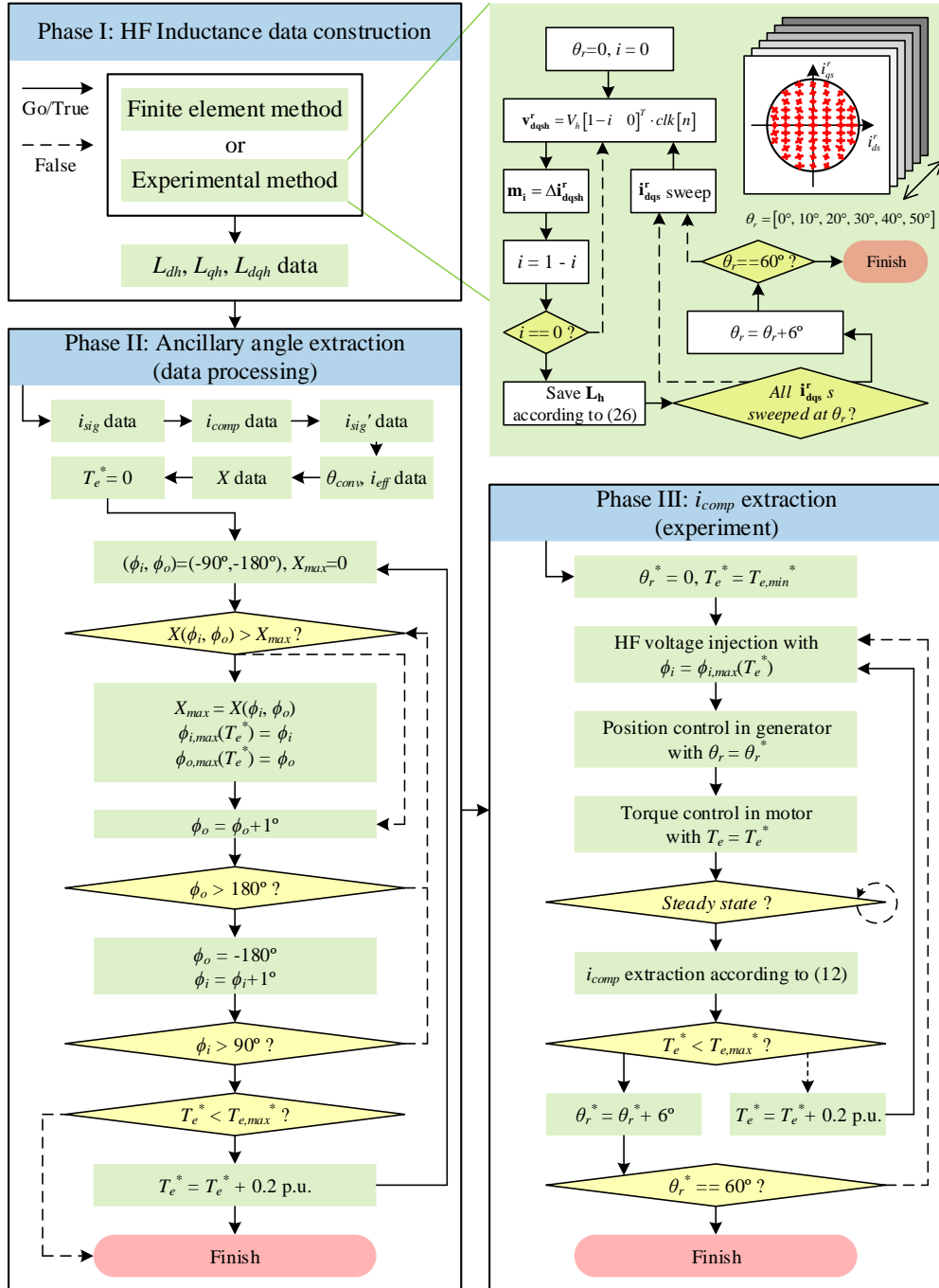


Fig. 15. Flowchart of data processing algorithm for proposed method.

### B. Phase I: HF Inductance Data Construction

HF inductance data should be obtained in advance to extract the ancillary angles. There are two main methods to obtain such data. One is FEA and the other is experiment with HF voltage injection. Choosing the latter, HF voltage is injected into the  $d$ -axis of RRF as follows:

$$\mathbf{v}_{dqs}^r[n] = \begin{bmatrix} V_h \\ 0 \end{bmatrix} \cdot \mathbf{clk}[n]. \quad (20)$$

The current response would appear as follows:

$$\Delta \mathbf{i}_{dqs}^r[n] = V_h T_s \mathbf{L}_h^{-1} \begin{bmatrix} 1 \\ 0 \end{bmatrix} \cdot \mathbf{clk}[n-2]. \quad (21)$$

Let's define  $\mathbf{m}_i$  as the HF current deviation induced by the HF voltage, where subscript  $i$  is either 0 or 1.  $\mathbf{m}_0$  and  $\mathbf{m}_1$  are for the cases of  $d$ - and  $q$ -axis injections, respectively.  $\mathbf{m}_0$  can be deduced as follows:

$$\mathbf{m}_0[n] = \Delta \mathbf{i}_{dqs}^r[n] \cdot \mathbf{clk}[n-2] = V_h T_s \mathbf{L}_h^{-1} \begin{bmatrix} 1 \\ 0 \end{bmatrix} \cdot \mathbf{clk}[n-2]. \quad (22)$$

After  $\mathbf{m}_0$  is stored in the memory of control computer, HF voltage is injected into the  $q$ -axis of RRF as follows:

$$\mathbf{v}_{dqs}^r[n] = \begin{bmatrix} 0 \\ V_h \end{bmatrix} \cdot \mathbf{clk}[n]. \quad (23)$$

The current deviation by the  $q$ -axis HF voltage appears as follows:

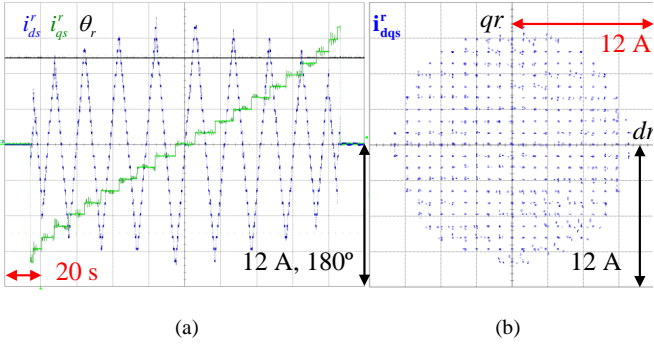


Fig. 16. (a) Waveform and (b) x-y plot when extracting experimental HF inductance data.

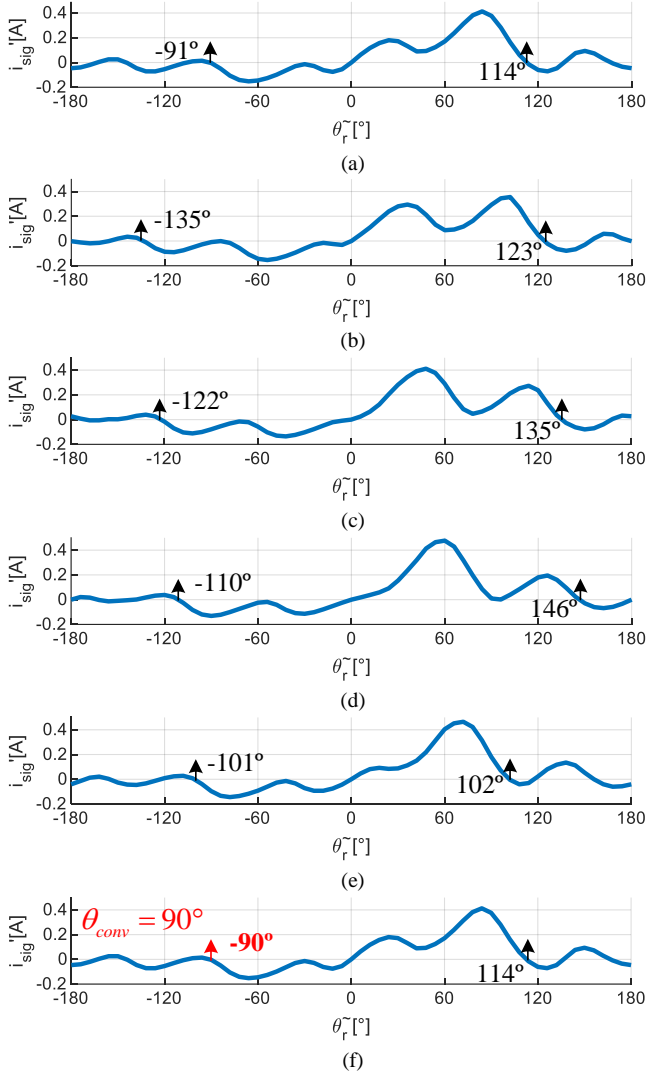


Fig. 17. (a)  $i_{sig}'$  graphs at various rotor positions with zero down crossing points at  $\tilde{\theta}_r = 0^\circ$ , (b)  $10^\circ$ , (c)  $20^\circ$ , (d)  $30^\circ$ , (e)  $40^\circ$ , and (f)  $50^\circ$  ( $T_e^* = 2$  pu,  $\phi_i = 51^\circ$ , and  $\phi_o = -90^\circ$ ).

$$\Delta \mathbf{i}_{dqsh}^r[n] = V_h T_s \mathbf{L}_h^{-1} \begin{bmatrix} 0 \\ 1 \end{bmatrix} \cdot clk[n-2], \quad (24)$$

and then  $\mathbf{m}_1$  is derived as follows:

$$\mathbf{m}_1[n] = \Delta \mathbf{i}_{dqsh}^r[n] \cdot clk[n-2] = V_h T_s \mathbf{L}_h^{-1} \begin{bmatrix} 0 \\ 1 \end{bmatrix} \cdot clk[n-2]. \quad (25)$$

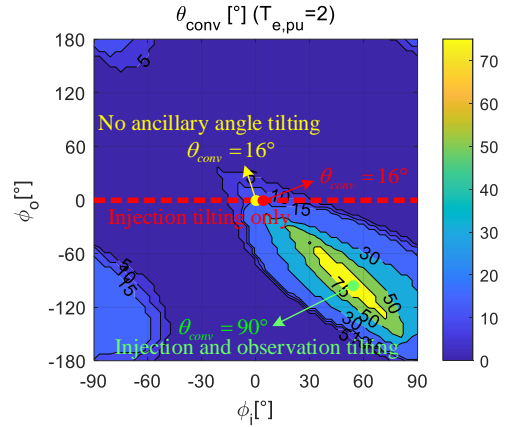


Fig. 18. Contour map of  $\theta_{conv}$  according to  $\phi_i$  and  $\phi_o$  with  $T_e^* = 2$  pu.

$\mathbf{m}_0$  and  $\mathbf{m}_1$  should be extracted several times and averaged to minimize effect of sampling error. On the other hand, if large current continuously flows through the stator winding for a long time, the stator coil could be excessively heated up. Therefore, the experiment should be conducted for an appropriate duration and within a proper current operating range.

Since the HF inductances should be obtained according to the current operating points and rotor positions, the target motor current should be controlled at a fixed rotor position. Therefore, the target motor and the load machine perform current control and position control, respectively. Fig. 16 shows the waveform of current sweep at a fixed  $\theta_r$  for HF inductance extraction. This work should be repeated at the different  $\theta_r$ .

By solving (22) and (25) simultaneously,  $\mathbf{L}_h$  can be obtained with stored  $\mathbf{m}_0$  and  $\mathbf{m}_1$  as follows:

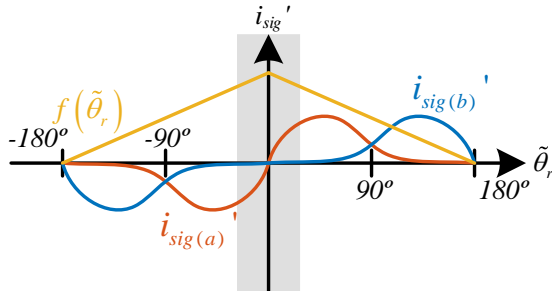
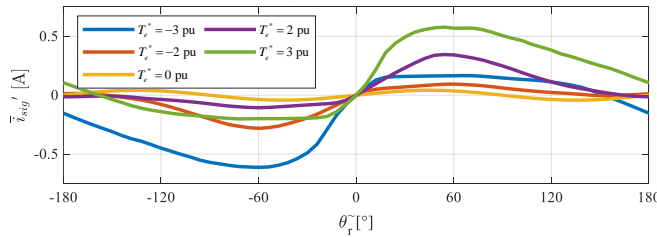
$$\mathbf{L}_h = V_h T_s [\mathbf{m}_0 \ \mathbf{m}_1]^{-1} \cdot clk[n-2]. \quad (26)$$

$\mathbf{L}_h$  is defined in a three-dimensional domain,  $i_{ds}^r$ ,  $i_{qs}^r$ , and  $\theta_r$ . Each component of  $\mathbf{L}_h$  will be processed to obtain optimal ancillary angles in *Phase II*. The experimental results of HF inductance extraction will be shown in Chapter IV.

### C. Phase II: Ancillary Angle Extraction

The look-up table (LUT) of  $\phi_i$  and  $\phi_o$  should be pre-calculated before a drive with the proposed SISC algorithm. In this paper, the strategy for improving dynamic performance is to define an index that quantifies SISC characteristics and maximize the index. The optimal  $\phi_i$  and  $\phi_o$  at each torque are selected by maximizing the index in the proposed method. The index is named ‘performance index’ throughout this paper, expressed as  $X(\phi_i, \phi_o)$  which is a function of the ancillary angles. All calculations in *Phase II* are conducted on MATLAB with HF inductance data extracted from *Phase I*.

$i_{sig}$  is derived from  $\mathbf{L}_h$ ,  $\phi_i$ , and  $\phi_o$ . The target current operating point is limited on maximum torque per ampere (MTPA) trajectory, so  $i_{sig}$  and  $i_{sig}'$  are functions of  $T_e^*$ ,  $\tilde{\theta}_r$ ,  $\theta_r$ ,  $\phi_i$ , and  $\phi_o$ . In (16)-(17), although  $\tilde{\theta}_r$  appears in the trigonometric functions of  $i_{sig}$ , it affects  $\phi_A$ ,  $I_A$ , and  $I_\Sigma$  because the actual operating current varies according to  $\tilde{\theta}_r$  as depicted in Fig. 2(b).  $i_{sig}'$  should be derived considering this observation. It will be used for extracting ancillary angles.

Fig. 19. Two examples of  $i_{sig}'$  to compare with.Fig. 20.  $\bar{i}_{sig}'$  curves with  $T_e^* = -3 \sim 3$  pu.

Before setting up the performance index, two additional sub-indexes are proposed in advance. First,  $\theta_{conv}$  is the minimum distance for the whole range of  $\theta_r$  from the major convergence point to the boundaries of the convergence range. It is defined as follows:

$$\theta_{conv} = \min(|\tilde{\theta}_r|) \text{ s.t. } i_{sig}'(\tilde{\theta}_r) = 0 \quad (27)$$

except for  $\tilde{\theta}_r = 0$ . If  $i_{sig}'$  is zero down-crossing at  $\tilde{\theta}_r = 0$  point,  $\theta_{conv}$  is set to 0 exceptionally because  $\tilde{\theta}_r$  cannot converge to  $\tilde{\theta}_r = 0$  point with negative feedback of the position tracking observer.

For example, Fig. 17 shows  $i_{sig}'$  graphs at various rotor positions with  $T_e^* = 2$  pu pinpointing zero down crossing points. According to (27),  $\theta_{conv}$  becomes  $90^\circ$  in the case of Fig. 17, which is the minimum absolute angle among the pinpointed angles.

Fig. 18 represents the contour map of  $\theta_{conv}$  according to  $\phi_i$  and  $\phi_o$  with  $T_e^* = 2$  pu. In the figure, the yellow point and the red line represent the ancillary angle composition of the conventional SISC algorithms in [13] and [17], respectively. In [13], HF voltage is injected, HF current is processed within ERRF, and convergence points are manipulated with  $i_{comp}$ . Therefore, this conventional method does not use any ancillary angles, i.e.,  $(\phi_i, \phi_o) = (0,0)$ , in the entire torque region. Meanwhile, voltage injection and signal processing are conducted within AIRF in [17]. This conventional method exploits  $\phi_i$  tilting only and fixes  $\phi_o$  to  $0^\circ$ . The maximum  $\theta_{conv}$  is limited to  $16^\circ$  on the red line for the case of  $T_e^* = 2$  pu. However,  $\theta_{conv}$  can be maximized up to  $90^\circ$  in the entire plane at  $(\phi_i, \phi_o) = (54^\circ, -90^\circ)$ . Since  $i_{sig}'$  has the symmetric characteristics,  $i_{sig}'$  has the following feature:

$$i_{sig}'(T_e^*, \theta_r, \tilde{\theta}_r) = i_{sig}'\left(-T_e^*, \frac{\pi}{3} - \theta_r, -\tilde{\theta}_r\right). \quad (28)$$

Thus, the maximum  $\theta_{conv}$  with  $T_e^* = 2$  pu is identical to that

with  $T_e^* = -2$  pu. In sum, there are more options to conspicuously amplify the maximum value of the performance index by exploiting both  $\phi_i$  and  $\phi_o$ , unlike the conventional viewpoint where  $\phi_i$  is only taken into account.

Meanwhile, a larger current signal than disturbance components enables a more robust SISC algorithm [11]. Fig. 19 shows an example of zero-point symmetric  $i_{sig}'$  graphs named  $i_{sig(a)}$ ' and  $i_{sig(b)}$ '. Their average values are the same as follows:

$$i_{avg} = \frac{\int_0^{\theta_{conv}} i_{sig(a)}' d\tilde{\theta}_r}{\theta_{conv}} = \frac{\int_0^{\theta_{conv}} i_{sig(b)}' d\tilde{\theta}_r}{\theta_{conv}}. \quad (29)$$

$i_{avg}$  is the average value of  $i_{sig}'$  from  $0^\circ$  to  $\theta_{conv}$ . However,  $i_{sig(b)}'$  near the  $\tilde{\theta}_r = 0^\circ$  line indicated within the grey shadow area is small compared to  $i_{sig(a)}'$ . In the case of  $i_{sig(b)}'$ , the input signal of the observer will be dominated by highly random disturbance components. Hence,  $i_{sig}'$  near the major convergence point is crucial.

A weight function expressed as  $f(\tilde{\theta}_r)$  is taken into account, and it is drawn as the yellow graph in Fig. 19, which can quantify the magnitude of  $i_{sig}'$  near the major convergence point.  $f(\tilde{\theta}_r)$  decreases as  $\tilde{\theta}_r$  goes further from  $0^\circ$ .  $f(\tilde{\theta}_r)$  is multiplied to each of  $i_{sig}'$ , integrated, and divided by the integral of  $f(\tilde{\theta}_r)$ , which finally derives the weighted average as follows:

$$\frac{\int_0^{\theta_{conv}} f(\tilde{\theta}_r) i_{sig(a)}' d\tilde{\theta}_r}{\int_0^{\theta_{conv}} f(\tilde{\theta}_r) d\tilde{\theta}_r} > i_{avg} > \frac{\int_0^{\theta_{conv}} f(\tilde{\theta}_r) i_{sig(b)}' d\tilde{\theta}_r}{\int_0^{\theta_{conv}} f(\tilde{\theta}_r) d\tilde{\theta}_r}. \quad (30)$$

The weighted averages of both  $i_{sig}'$  have different values.  $i_{sig(a)}'$  has a larger weighted average than  $i_{sig(b)}'$ , meaning that  $i_{sig(a)}'$  has a stronger signal that is robust to the observer input disturbance than  $i_{sig(b)}'$ . The weighted average of  $i_{sig}'$  in (30) quantifies the robustness; thus, it can be exploited as a essential sub-index.

Meanwhile,  $i_{sig}'$  shows other peculiar characteristics in heavy loading condition. For simple discussion, the variation of  $i_{sig}'$  due to the spatial harmonics is neglected, and  $i_{sig}'$  is replaced by  $\bar{i}_{sig}'$  derived as follows:

$$\bar{i}_{sig}'(\tilde{\theta}_r) = \frac{3}{\pi} \int_0^{\pi/3} i_{sig}' d\theta_r. \quad (31)$$

$\bar{i}_{sig}'$  is averaged  $i_{sig}'$  for a  $60^\circ$  interval due to the periodicity.

Fig. 20 shows the graphs of  $\bar{i}_{sig}'$  with different torques and corresponding ancillary angles. This figure depicts that the graph of  $\bar{i}_{sig}'$  with  $T_e^* = 0$  pu is sinusoidal and thus zero-point symmetric. However, with  $T_e^* = 2$  pu and  $T_e^* = 3$  pu, the magnitude of the valley of the graph is smaller than that of the peak. Conversely, this phenomenon is completely reversed for the peak and the valley of  $\bar{i}_{sig}'$  with  $T_e^* = -2$  pu and  $T_e^* = -3$  pu.  $i_{sig}'$  is influenced by many factors, including the HF inductances, the combination of  $\phi_i$ ,  $\phi_o$ , and  $i_{comp}$ . Thus, it is complex to generalize the characteristics of  $i_{sig}'$ . However, there are certain imbalances of  $i_{sig}'$  magnitude depending on the sign of  $\tilde{\theta}_r$ .

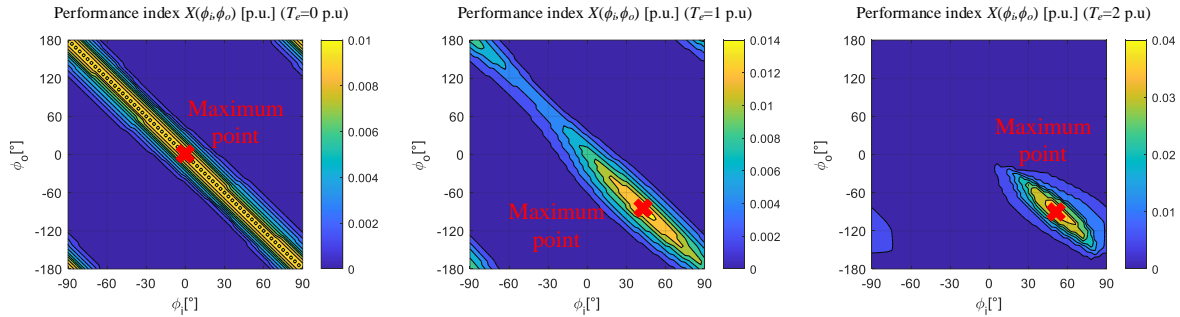
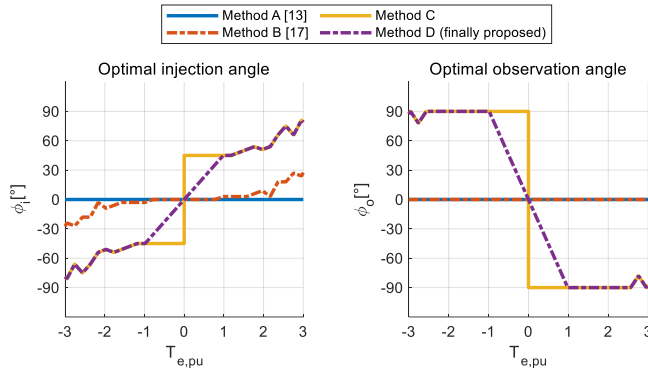
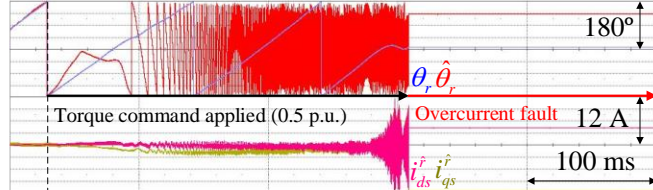
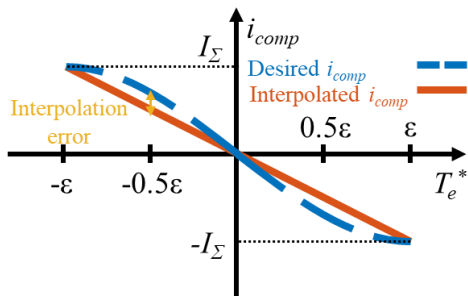
Fig. 21. Contour maps of performance indexes with  $T_e^* = 1 \sim 3$  pu.

Fig. 22. Extracted LUTs of ancillary angles with various methods.

Fig. 23. Experiment result with LUT extracted with proposed method without limiting angle slope (200 r/min,  $T_e^* = 0.5$  pu).Fig. 24. Interpolation error of  $i_{comp}$  near  $T_e^* = 0$  with Method C.

For these reasons,  $i_{eff}$ , the secondary sub-index, will be derived with a geometric average of two effective signals of different signs as follows:

$$i_{eff} = \sqrt{i_{eff+} \cdot i_{eff-}} \quad (32)$$

where

$$i_{eff+} = \frac{\int_{-\theta_{conv}}^{0} (\theta_{conv} - \tilde{\theta}_r) \cdot \bar{i}_{sig} \cdot d\tilde{\theta}_r}{\int_{-\theta_{conv}}^{0} (\theta_{conv} - \tilde{\theta}_r) d\tilde{\theta}_r}, \quad (33)$$

and

$$i_{eff-} = \frac{\int_{-\theta_{conv}}^{0} (\theta_{conv} + \tilde{\theta}_r) \cdot \bar{i}_{sig} \cdot d\tilde{\theta}_r}{\int_{-\theta_{conv}}^{0} (\theta_{conv} + \tilde{\theta}_r) d\tilde{\theta}_r}. \quad (34)$$

In (32),  $i_{eff}$  is derived from the geometric average of  $i_{eff+}$  and  $i_{eff-}$ . Note that the geometric average gives more weight to a smaller value. Eq. (33)-(34) are the weighted averages for positive and negative  $\tilde{\theta}_r$ , respectively. The weight function in (33)-(34) is the distance from the minor convergence point of each side to the major convergence point.

Finally, the performance index is defined with  $\theta_{conv}$  and  $i_{eff}$  as follows:

$$X = \theta_{conv} \cdot i_{eff} \quad (35)$$

In (35), the product operation has an advantage in that the complexity of normalization is reduced. It plays a role as the digital ‘AND’ operation, allowing  $X$  to be large only if all operands are large enough. This is because both  $\theta_{conv}$  and  $i_{eff}$  should have large values for better SISC performance. For example, a small effective signal could become too sensitive to disturbances, even if the convergence range is stretched with sufficient  $\theta_{conv}$ . In contrast, despite sufficiently large  $i_{eff}$ , a narrow convergence range limits the dynamic SISC operation because  $\tilde{\theta}_r$  can easily diverge with a slight displacement of itself. For different values of  $T_e^*$ , contour maps of the performance index  $X$  are expressed in Fig. 21. The combination of ancillary angles which maximizes  $X$  will become the components of LUT finally used for the proposed method.

Fig. 23 shows the experimental result of torque control with gently increasing torque command using the LUT of ‘Method C’ in Fig. 22.  $\hat{\theta}_r$  diverges in the transient as soon as positive torque command is applied. The result is not consistent with the previous analysis.

#### D. Minimization of Interpolation Error

Fig. 23 shows the experimental result of torque control with gently increasing torque command using the LUT of ‘Method C’ in Fig. 22.  $\hat{\theta}_r$  diverges in the transient as soon as positive torque command is applied. The result is not consistent with the previous analysis.

Before analyzing and solving the divergence problem, it is presumed that HF inductance and related functions, such as  $I_\Sigma$ , are the same for all torques and rotor positions in a low torque

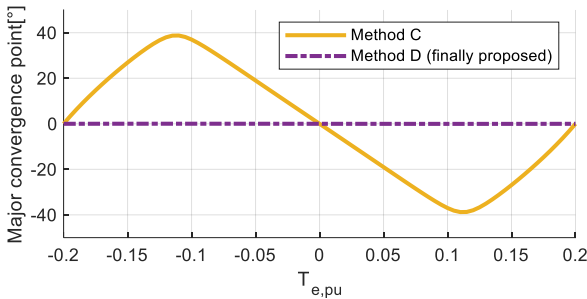
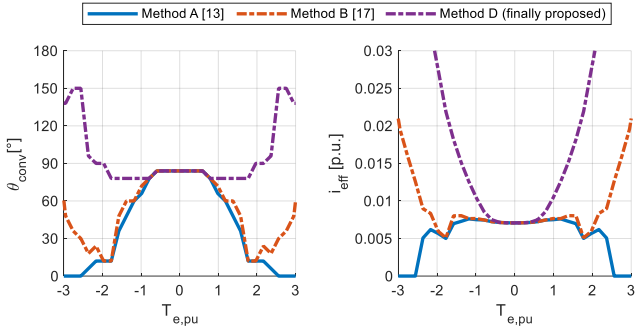
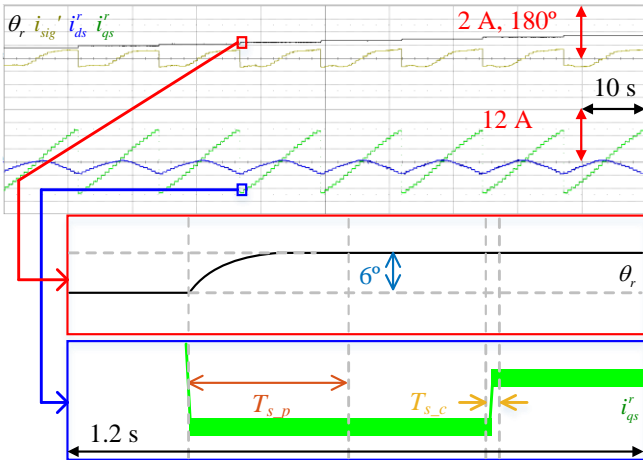


Fig. 25. Major convergence point with ‘Method C’ and ‘Method D’.

Fig. 26. Sub-indexes ( $\theta_{\text{conv}}, i_{\text{eff}}$ ) for various LUT composition.Fig. 27. Experimental waveforms when  $i_{\text{comp}}$  is extracted.

region where the inductances merely vary. Moreover,  $\phi_a$  is assumed to be 0 due to negligible cross-saturation in the low torque region.

As shown in ‘Method C’ graph in Fig. 22,  $\phi_i$  and  $\phi_o$  have discontinuous points at  $T_e^* = 0$ . According to (16), due to the abrupt change of  $\phi_i$  and  $\phi_o$  for ‘Method C’ with  $T_e^* = 0$  pu, the dc offset of  $i_{\text{sig}}$  also varies stepwise from 0 to  $I_\Sigma$  as  $T_e^*$  changes from 0 to 0+. Therefore, desired  $i_{\text{comp}}$  with  $T_e^* = 0+$  is  $-I_\Sigma$  while  $i_{\text{comp}}$  with  $T_e^* = 0$  is zero.

In this case, the discontinuity of  $i_{\text{comp}}$  can degrade the accuracy of interpolation. Fig. 24 shows how the interpolation error is made, where the discrete input interval of LUT is marked as  $\varepsilon$ . Note that  $\varepsilon$  is set as 0.2 pu torque in this paper. According to (16), the dc offset of  $i_{\text{sig}}$  with  $|T_e^*| < \varepsilon$  for ‘Method C’ is  $I_\Sigma \sin(\pi T_e^* / 2\varepsilon)$ , thus, the desired  $i_{\text{comp}}$  is determined as

$-I_\Sigma \sin(\pi T_e^* / 2\varepsilon)$ . However, the interpolated  $i_{\text{comp}}$  is  $-I_\Sigma T_e^* / \varepsilon$ . Therefore, the interpolation error exists with  $|T_e^*| < \varepsilon$ , locating the major convergence points to the undesired points.

Fig. 25 shows the major convergence points of ‘Method C’ and ‘Method D’ with  $|T_e^*| \leq \varepsilon$ . The major convergence point of ‘Method C’ fluctuates up to 39° with  $T_e^* = -0.55\varepsilon$ , which deteriorates SISC performance with a large tracking error. Besides, the large variation of  $\phi_i$  and  $\phi_o$  near  $T_e^* = 0$  in the case of ‘Method C’ can induce a large transient error, which acts as a additional disturbance to the position tracking observer. It can also undermine the dynamic performances of SISC using ‘Method C’. However, the major convergence point of ‘Method D’ is almost 0° regardless of  $T_e^*$ .

To solve above transient error, smoother changes of  $\phi_i$  and  $\phi_o$  at zero torque are required. If  $2\phi_i + \phi_o$  is the same,  $i_{\text{sig}}'$  does not vary regardless of the ancillary angles by considering (16)-(17), providing that HF inductance does not vary in the low torque region. Therefore, discontinuity problems can be solved by keeping  $2\phi_i + \phi_o$  equal but changing  $\phi_i$  and  $\phi_o$  smoothly without a discontinuous point at  $T_e^* = 0$ .

With these considerations, the graphs of ‘Method D’ in Fig. 22 are finally chosen for LUTs of  $\phi_i$  and  $\phi_o$ . With  $|T_e^*| < 1$  pu, ancillary angles of ‘Method D’ change gradually, eliminating the discontinuity problems with  $T_e^* = 0$ . Note that  $\phi_i$  and  $\phi_o$  are smoothed only with  $|T_e^*| < 1$  pu, which guarantees maximum performance index in the high torque region,  $|T_e^*| \geq 1$  pu.

Fig. 26 shows sub-indexes derived for three different methods discussed in Fig. 22.  $\theta_{\text{conv}}$  and  $i_{\text{eff}}$  of ‘Method A’ are the smallest among the other methods. Even though the sub-indexes are improved by ‘Method B’, the performance is not satisfactory in the range,  $1 \text{ pu} < |T_e^*| < 2 \text{ pu}$ . On the contrary, ‘Method D’ has the largest sub-indexes among the methods. ‘Method D’ achieved remarkably high sub-indexes by utilizing the ancillary angles in the higher torque region. Also, in the lower torque region, the performance is not degraded due to graded the ancillary angles.

#### E. Phase III: Compensation Current ( $i_{\text{comp}}$ ) Extraction

$i_{\text{comp}}$  can be calculated with HF inductance data from *Phase I*. However, it is more precise to extract  $i_{\text{comp}}$  in the real SISC working condition with experiment. Fig. 27 shows the waveforms of  $\theta_r$ ,  $i_{\text{sig}}'$ ,  $i_{ds}'$ , and  $i_{qs}'$ , in *Phase III* sequence. First, the load machine aligns the target motor to the specific  $\theta_r$  under position control. After that, the current command is sequentially modified according to the MTPA trajectory. After sampling  $i_{\text{sig}}$  on the MTPA trajectory for a specific position, the rotor position is altered by 6°. According to (11),  $i_{\text{comp}}$  can be derived with  $i_{\text{sig}}'$  data.

In Fig. 27,  $T_{s,p}$  is a settling time of the position control. Since  $i_{\text{sig}}$  should be sampled only when the rotor position is fixed,  $i_{\text{sig}}$  is sampled after  $T_{s,p}$ . In addition, there is also a settling time for the current,  $T_{s,c}$ , where the processor does not sample  $i_{\text{sig}}$  and awaits until the current is settled.

## IV. EXPERIMENTAL RESULTS

An experiment is conducted to evaluate the dynamic performance of the conventional and the proposed SISC methods at high-loading conditions. In this experiment, the conventional SISC and the proposed SISC exploit the LUT of

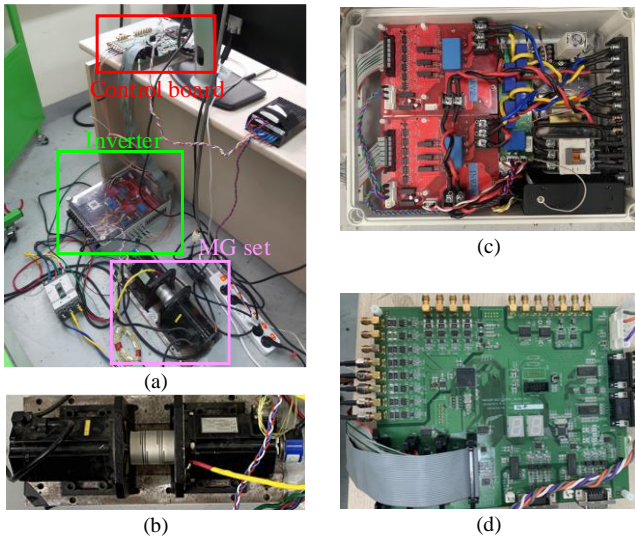


Fig. 28. Driver platforms: (a) experimental set-up, (b) motor-generator set, (c) inverters, and (d) control board for experiment.

Table III. Specification of control variables.

$f_{cc}$	500 Hz
$\zeta_{NF}$	0.3
$f_{c,NF}$	5 kHz
Observer type	Luenberger observer
$f_{obs}$	$-14.1+j14.1$ Hz, -25 Hz
$V_h$	40 V
$f_h$	5 kHz
$f_{sw}$	10 kHz
$f_s$	20 kHz

$\phi_i$  and  $\phi_o$  shown as ‘Method B’ and ‘Method D’ in Fig. 22, respectively. In the experiments, the load machine is driven under speed control mode at 200 r/min. In the experiment, a motor-generator set, an inverter, and a control board shown in Fig. 28 are used. Some control parameters used in the experiments are shown in Table III.  $f_{cc}$ ,  $\zeta_{NF}$ , and  $f_{c,NF}$  are bandwidth of current control, damping coefficient, and cutoff frequency of notch filter, respectively.  $f_{obs}$  is a pole of the position observer. Luenberger observer used is a third order observer, so it has three poles.  $V_h$ ,  $f_h$ ,  $f_{sw}$ , and  $f_s$  are HF injection voltage, injection frequency, switching frequency, and sampling frequency, respectively.

Fig. 29 shows the experimental results of extracted HF inductances obtained with the method illustrated in *Phase I*. Both FEA data shown in Fig. 4 and the experimental data shown in Fig. 29 can be employed for ancillary angle extraction.

In Fig. 30, the robustness of the proposed method to a stepwise torque is verified. 2 pu torque command has been applied at 0.1 s, the command goes to zero at 0.4 s, and it goes down to  $-2$  pu at 0.6 s. Target motor is under current control, and load machine is under speed control. As shown in Fig. 30(a), after 2 pu torque is applied at a standstill,  $\hat{\theta}_r$  has a large error. Then, after 0 pu torque is applied,  $\hat{\theta}_r$  re-converges to the actual position. On the other hand, Fig. 30(b) shows that the position is continuously well estimated with the proposed method even if  $\pm 2$  pu torque is exerted stepwise. When the motor rotates at

50 r/min, the position tracking capability is also lost under  $\pm 2$  pu torque as shown in Fig. 30(c). However, Fig. 30(d) shows that SISC works well with the proposed method. Under a speed control condition of 200 r/min,  $\hat{\theta}_r$  starts to diverge from  $t = 0.65$  s after applying  $-2$  pu torque and wholly loses position tracking capability in response to  $-2$  pu step torque for ‘Method B’, as shown in Fig. 30(e). However, in Fig. 30(f), the sensorless algorithm works well thanks to the proposed SISC method. Fig. 31 shows how the position error point moves on the  $i_{sig}$ ’ contour map in Fig. 30 (a). A white triangle indicates the initial operating point, and the face color of the triangle gets gradually darker as time goes by. Tagged numbers from 1 to 18 near the arrows represent some instants from 0.6 s to 0.67 s in the experiment with the conventional method. From points 1 to 6,  $\hat{\theta}_r$  is pushed to the minor convergence point due to the disturbance coming from the rapid current variation. After that, from point 7,  $\hat{\theta}_r$  is trapped at the minor convergence point. As the motor rotates in the positive direction, the minor convergence point where  $\hat{\theta}_r$  is trapped gradually moves away from  $0^\circ$ . After the motor rotates two times, at point 13,  $\hat{\theta}_r$  arrives at the more outlying convergence point than at point 7. After point 13,  $\hat{\theta}_r$  moves further away from  $0^\circ$  and eventually diverges. This divergence pattern fits in the trajectory depicted in Fig. 8.

Fig. 32 shows relationship between index  $X$  and SISC performance with experimental results of  $\pm 2$  pu stepwise torque control at 200 r/min with arbitrary combinations of ancillary angles.  $X$  values of Fig. 32(a), (b), and (c) are  $X_a$ ,  $X_b$ , and  $X_c$ , respectively.  $X_a < X_b < X_c$  in the entire torque region. Therefore, it is expected that SISC performance of case (a) is inferior to those of cases (b), (c), and that of case (c) is superior to the others. As shown in Fig. 32(a), SISC fails even at 2 pu torque. However, in case (b) shown in Fig. 32(b),  $\hat{\theta}_r$  well tracks  $\theta_r$  at 2 pu torque, but it diverges at  $-2$  pu torque. However, as shown in Fig. 32(c), the best SISC performance can be seen, and position tracking capability is well kept at both  $\pm 2$  pu torque.

## V. CONCLUSION

This paper analyzes the convergence of IPMSM SISC. The proposed method uses ancillary angles, injection, and observation angles. A variable gain connecting the HF current to position error has been newly defined to reflect the variation of the dynamic inductance of IPMSM under magnetic saturation. Moreover, the extraction method of ancillary angle in LUT is also proposed to exploit the SISC algorithm, reflecting the SISC performance. The proposed method solved the problem of the divergence of the position tracking observer under severely saturated IPMSM. The superiority of the proposed method was verified with the experiments. The robustness of the proposed method was also confirmed by applying stepwise torque. The observer tracked well the position under highly saturated IPMSM in the proposed SISC.

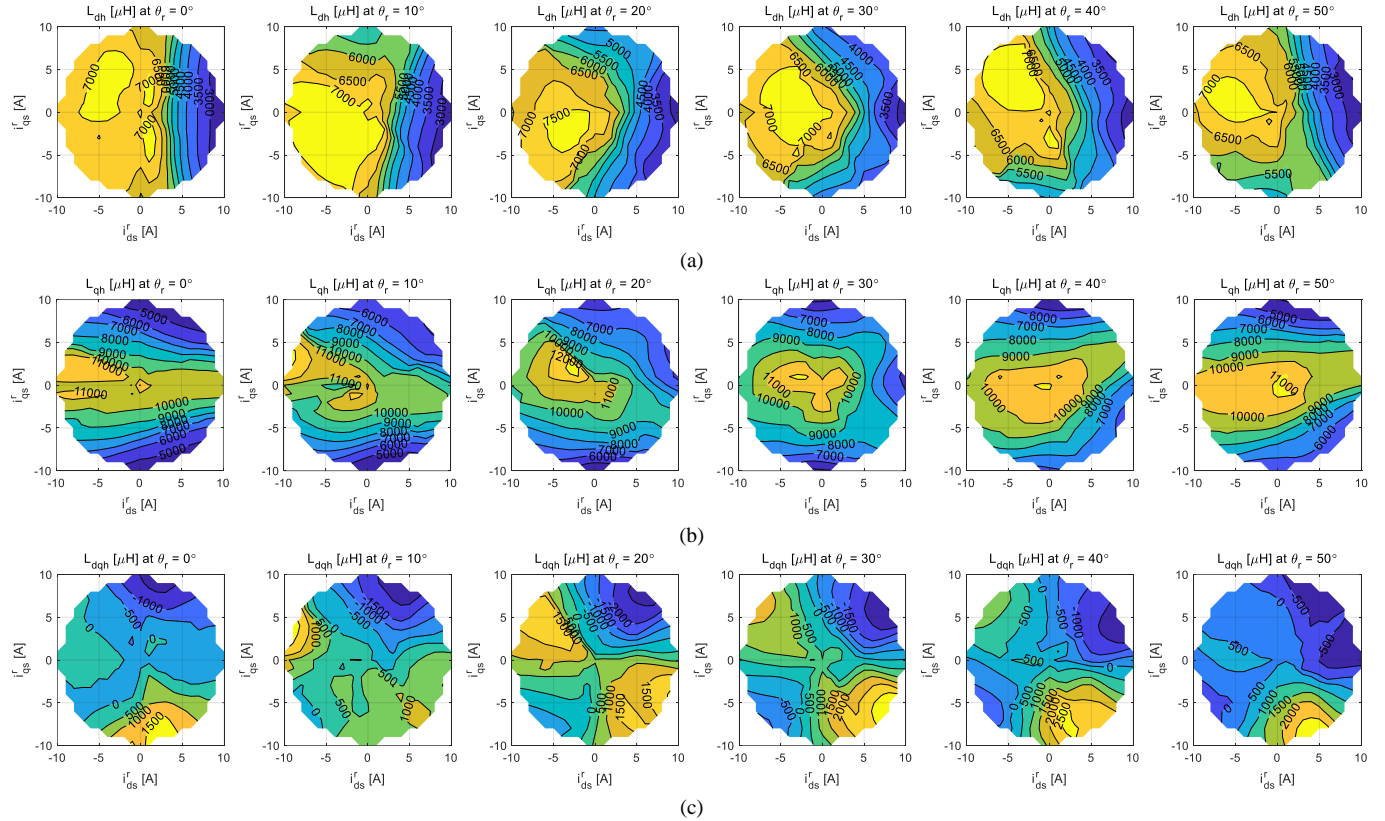


Fig. 29. (a)  $L_{dh}$ , (b)  $L_{qh}$ , and (c)  $L_{dqh}$  contours of target IPM (experiment).

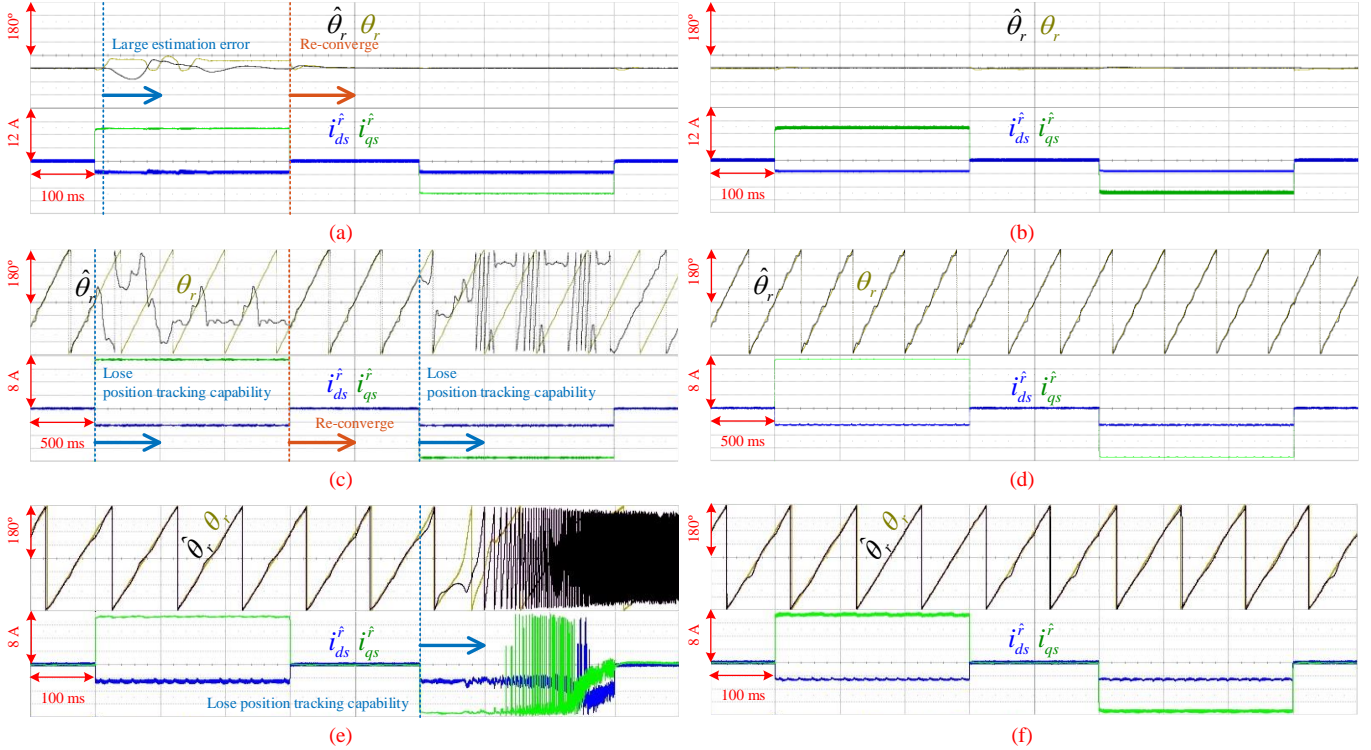


Fig. 30. Torque control experiment with  $T_e^* = \pm 2$  pu. (a) Standstill with conventional SISC, and (b) standstill with proposed SISC. (c) 50 r/min with conventional SISC, and (d) 50 r/min with proposed SISC. (e) 200 r/min with conventional SISC, and (f) 200 r/min with proposed SISC.

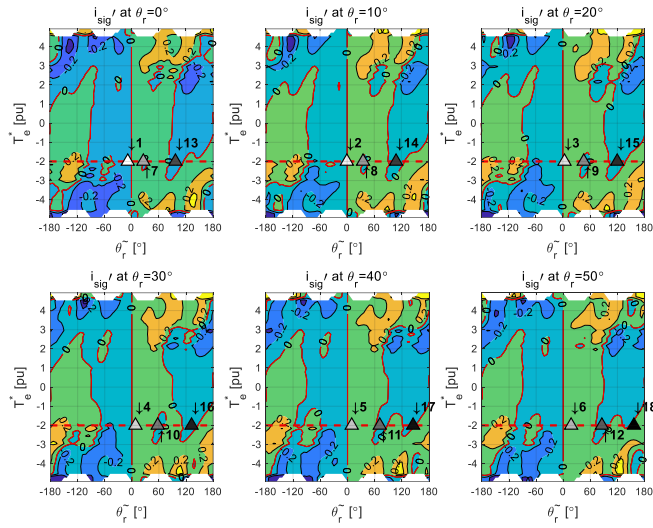


Fig. 31. Torque control experiment: (a) conventional SISC, and (b) proposed SISC with  $T_e^* = \pm 2$  pu at 200 r/min.

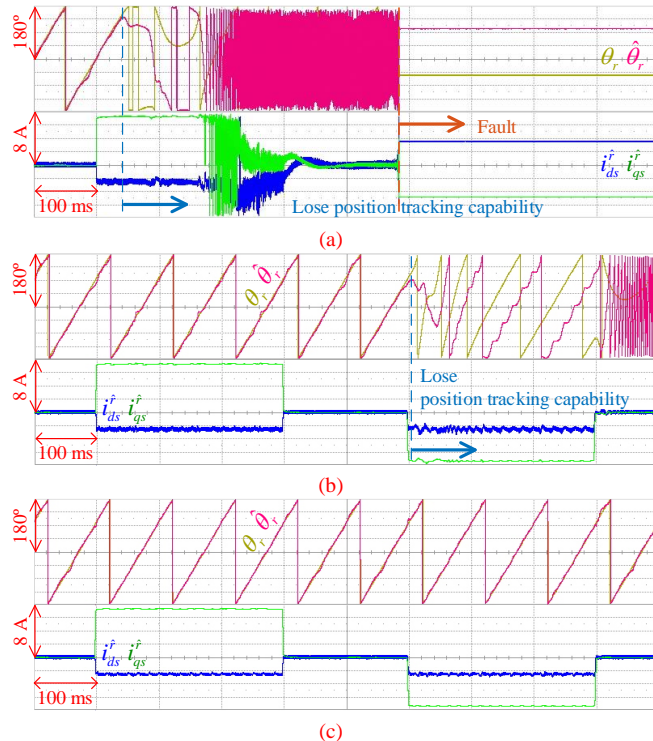


Fig. 32. Torque control experiment with  $T_e^* = \pm 2$  pu at 200 r/min according to different combinations of ancillary angles with proposed method. (a) Case with  $X = X_a$ . (b) Case with  $X = X_b$ . (c) Case with  $X = X_c$ . ( $X_a < X_b < X_c$ )

## REFERENCES

- [1] Y. D. Yoon, S. K. Sul, S. Morimoto, and K. Ide, "High-bandwidth sensorless algorithm for AC machines based on square-wave-type voltage injection," *IEEE Trans. Ind. Appl.*, vol. 47, no. 3, pp. 1361-1370, May/Jun. 2011.
- [2] S. Morimoto, K. Kawamoto, M. Sanada and Y. Takeda, "Sensorless control strategy for salient-pole PMSM based on extended EMF in rotating reference frame," *IEEE Trans. Ind. Appl.*, vol. 38, no. 4, pp. 1054-1061, Jul./Aug. 2002.
- [3] N. Matsui, "Sensorless PM brushless DC motor drives," in *IEEE Trans. Ind. Electron.*, vol. 43, no. 2, pp. 300-308, Apr. 1996.
- [4] Y. C. Kwon, J. Lee and S. K. Sul, "Recent advances in sensorless drive of interior permanent-magnet motor based on pulsating signal injection," *IEEE Trans. Emerg. Sel. Topics Power Electron.*, vol. 9, no. 6, pp. 6577-6588, Dec. 2021.
- [5] D. Mingardi, M. Morandin, S. Bolognani and N. Bianchi, "On the properties of the differential cross-saturation inductance in synchronous machines," in *IEEE Trans. Ind. Appl.*, vol. 53, no. 2, pp. 991-1000, Mar./Apr. 2017.
- [6] M. Berto, L. Alberti, V. Manzolini and S. Bolognani, "Computation of self-sensing capabilities of synchronous machines for rotating high frequency voltage injection sensorless control," *IEEE Trans. Ind. Electron.*, vol. 69, no. 4, pp. 3324-3333, Apr. 2022.
- [7] N. Bianchi, E. Fornasiero and S. Bolognani, "Effect of stator and rotor saturation on sensorless rotor position detection," *IEEE Trans. Ind. Appl.*, vol. 49, no. 3, pp. 1333-1342, May/Jun. 2013.
- [8] P. Guglielmi, M. Pastorelli and A. Vagati, "Cross-saturation effects in IPM Motors and related impact on Sensorless Control," *IEEE Trans. Ind. Appl.*, vol. 42, no. 6, pp. 1516-1522, Nov./Dec. 2006.
- [9] N. Bianchi and S. Bolognani, "Influence of rotor geometry of an IPM motor on sensorless control feasibility," *IEEE Trans. Ind. Appl.*, vol. 43, no. 1, pp. 87-96, Jan./Feb. 2007.
- [10] P. Sergeant, F. De Belie and J. Melkebeek, "Rotor geometry design of interior PMSMs with and without flux barriers for more accurate sensorless control," *IEEE Trans. Ind. Electron.*, vol. 59, no. 6, pp. 2457-2465, Jun. 2012.
- [11] Y. C. Kwon and S. K. Sul, "Reduction of injection voltage in signal injection sensorless drives using a capacitor-integrated inverter," *IEEE Trans. Power Electron.*, vol. 32, no. 8, pp. 6261-6274, Aug. 2017.
- [12] C. E. Hwang, Y. Lee and S. K. Sul, "Analysis on position estimation error in position-sensorless operation of IPMSM using pulsating square wave signal injection," *IEEE Trans. Ind. Appl.*, vol. 55, no. 1, pp. 458-470, Jan./Feb. 2019.
- [13] Y. Lee, Y. C. Kwon, S. K. Sul, N. A. Baloch, and S. Morimoto, "Compensation of position estimation error for precise position-sensorless control of IPMSM based on high-frequency pulsating voltage injection," in *Proc. IEEE Energy Convers. Congr. Expo.*, Oct. 2017, pp. 859-864.
- [14] Y. Li, Z. Q. Zhu, D. Howe, C. M. Bingham and D. A. Stone, "Improved rotor-position estimation by signal injection in brushless AC motors, accounting for cross-coupling magnetic saturation," *IEEE Trans. Ind. Appl.*, vol. 45, no. 5, pp. 1843-1850, Sept./Oct. 2009.
- [15] V. Manzolini and S. Bolognani, "On the rotor position self-sensing capability of reluctance and IPM synchronous motors," *IEEE Trans. Ind. Appl.*, vol. 56, no. 4, pp. 3755-3766, Jul./Aug. 2020.
- [16] Z. Q. Zhu, Y. Li, D. Howe, and C. M. Bingham, "Compensation for rotor position estimation error due to cross-coupling magnetic saturation in signal injection based sensorless control of PM brushless AC motors," in *Proc. IEEE IEMDC*, 2007, vol. 1, pp. 208-213.
- [17] Y. C. Kwon, J. Lee and S. K. Sul, "Extending operational limit of IPMSM in signal-injection sensorless control by manipulation of convergence point," *IEEE Trans. Ind. Appl.*, vol. 55, no. 2, pp. 1574-1586, Mar./Apr. 2019.
- [18] J. Lee, Y. C. Kwon and S. K. Sul, "Signal-injection sensorless control with tilted current reference for heavily saturated IPMSMs," *IEEE Trans. Power Electron.*, vol. 35, no. 11, pp. 12100-12109, Nov. 2020.
- [19] T. Tuovinen and M. Hinkkanen, "Adaptive full-order observer with high-frequency signal injection for synchronous reluctance motor drives," *IEEE Trans. Emerg. Sel. Topics Power Electron.*, vol. 2, no. 2, pp. 181-189, Jun. 2014.
- [20] A. Varatharajan, G. Pellegrino and E. Armando, "Signal-injection sensorless control of synchronous reluctance machines for overload operation," *IEEE Trans. Power Electron.*, vol. 37, no. 5, pp. 5874-5883, May 2022.
- [21] Ji-Hoon Jang, S.-K. Sul, Jung-Ik Ha, K. Ide and M. Sawamura, "Sensorless drive of surface-mounted permanent-magnet motor by high-frequency signal injection based on magnetic saliency," *IEEE Trans. Ind. Appl.*, vol. 39, no. 4, pp. 1031-1039, Jul./Aug. 2003.

- [22] P. Guglielmi, M. Pastorelli, and A. Vagati, "Cross-saturation effects in IPM motors and related impact on sensorless control," *IEEE Trans. Ind. Appl.*, vol. 42, no. 6, pp. 1516–1522, Nov. 2006.
- [23] D. Mingardi, M. Morandin, S. Bolognani, and N. Bianchi, "On the proprieties of the differential cross-saturation inductance in synchronous machines," *IEEE Trans. Ind. Appl.*, vol. 53, no. 2, pp. 991–1000, Mar./Apr. 2017.
- [24] J. M. Liu and Z. Q. Zhu, "Novel sensorless control strategy with injection of high-frequency pulsating carrier signal into stationary reference frame," *IEEE Trans. Ind. Appl.*, vol. 50, no. 4, pp. 2574–2583, Jul./Aug. 2014.
- [25] P. Guglielmi, M. Pastorelli, and A. Vagati, "Impact of cross-saturation in sensorless control of transverse-laminated synchronous reluctance motors," *IEEE Trans. Ind. Electron.*, vol. 53, no. 2, pp. 429–439, Apr. 2006.
- [26] D. D. Reigosa, P. Garcia, F. Briz, D. Raca, and R. D. Lorenz, "Modeling and adaptive decoupling of high-frequency resistance and temperature effects in carrier-based sensorless control of PM synchronous machines," *IEEE Trans. Ind. Appl.*, vol. 46, no. 1, pp. 139–149, Jan./Feb. 2010.
- [27] R. W. Hejny and R. D. Lorenz, "Evaluating the practical low-speed limits for back-EMF tracking-based sensorless speed control using drive stiffness as a key metric," *IEEE Trans. Ind. Appl.*, vol. 47, no. 3, pp. 1337–1343, May/Jun. 2011.
- [28] S. C. Yang and R. D. Lorenz, "Surface permanent magnet synchronous machine position estimation at low speed using eddy-current-reflected asymmetric resistance," *IEEE Trans. Power Electron.*, vol. 27, no. 5, pp. 2595–2604, May 2012.
- [29] M. J. Corley and R. D. Lorenz, "Rotor position and velocity estimation for a permanent magnet synchronous machine at standstill and high speeds," *Conf. Rec. IEEE-IAS Annu. Meeting*, vol. 1, 1996, pp. 36–41.
- [30] K. Ide, J. K. Ha and M. Sawamura, "A hybrid speed estimation of flux observer for induction motor drives," *IEEE Trans. Ind. Electron.*, vol. 53, no. 1, Feb. 2006.
- [31] W. T. Villet, M. J. Kamper, P. Landsmann, and R. Kennel, "Evaluation of a simplified high frequency injection position sensorless control method for reluctance synchronous machine drives," in *Proc. IET PEMD 2012*, vol. 1, Bristol, UK, Mar. 2012, pp. 1–6.
- [32] S. Kuehl, P. Landsmann, and R. M. Kennel, "Compensating angle estimation errors caused by magnetic saturation in anisotropy-based sensorless control schemes," in *Proc. 3rd IEEE Int. Symp. Sensorless Control Elect. Drives*, 2012, pp. 1–6.